

manuscript submitted to *Water Resources Research*

1 **Real-time imaging reveals distinct pore scale dynamics**
2 **during transient and equilibrium subsurface multiphase**
3 **flow**

4 **Catherine Spurin¹, Tom Bultreys^{1,3}, Maja Rücker², Gaetano Garfi¹, Christian**
5 **M. Schlepütz⁴, Vladimir Novak⁴, Steffen Berg⁵, Martin J. Blunt¹& Samuel**
6 **Krevor¹**

7 ¹Department of Earth Science & Engineering, Imperial College London, UK

8 ²Department of Chemical Engineering, Imperial College London, UK

9 ³UGCT - PProGRess, Department of Geology, Ghent University, BE

10 ⁴Swiss Light Source, Paul Scherrer Institute, CH

11 ⁵Shell Global Solutions International B.V., NL

12 **Key Points:**

- 13 • We use synchrotron X-ray imaging to quantify the change in flow dynamics as the
14 system transitions to steady-state.
15 • We observed distinct dynamics during transient flow which would suggest that transi-
16 tient flow should be modelled with separate parameters.
17 • We quantify the timescales for steady-state to be established for different capillary
18 numbers and viscosity ratios.

Corresponding author: Catherine Spurin, c1s13@ic.ac.uk

19 **Abstract**

20 Many subsurface fluid flows, including the storage of CO₂ underground or the production of
 21 oil, are transient processes incorporating multiple fluid phases. The fluids are not in equilibrium meaning macroscopic properties such as fluid saturation and pressure vary in space
 22 and time. However, these flows are traditionally modelled with equilibrium (or steady-state)
 23 flow properties, under the assumption that the pore scale fluid dynamics are equivalent. In
 24 this work, we used fast synchrotron X-ray tomography with 1s time resolution to image the
 25 pore scale fluid dynamics as the macroscopic flow transitioned to steady-state. **For nitrogen**
 26 **or decane, and brine injected simultaneously into a porous rock we observed distinct pore**
 27 **scale fluid dynamics during transient flow.** Transient flow was found to be characterised
 28 by intermittent fluid occupancy, whereby flow pathways through the pore space were constantly rearranging. The intermittent fluid occupancy was largest and most frequent when
 29 a fluid initially invaded the rock. But as the fluids established an equilibrium the dynamics
 30 decreased to either static interfaces between the fluids or small-scale intermittent flow pathways,
 31 depending on the capillary number and viscosity ratio. If the fluids were perturbed
 32 after an equilibrium was established, by changing the flow rate, the transition to a new
 33 equilibrium was quicker than the initial transition. Our observations suggest that transient
 34 flows require separate modelling parameters. The timescales required to achieve equilibrium
 35 suggest that several metres of an invading plume front will have flow properties controlled
 36 by transient pore scale fluid dynamics.
 37

39 **1 Introduction**

40 Understanding the simultaneous flow of multiple fluids through the Earth's crust is a
 41 fundamental problem to our society. How fluids propagate, and become trapped, governs
 42 how safely CO₂ can be stored underground in saline aquifers to mitigate climate change
 43 (Rubin & De Coninck, 2005; Bachu, 2000; Bickle, 2009), if underground drinking water
 44 supplies will be protected from spilled non-aqueous contaminants (Pye & Patrick, 1983)
 45 and how much hydrocarbons will be produced from a reservoir (Blunt, 2017). The invasion
 46 of CO₂, or the contaminant, is a transient process; macroscopic fluid properties such as
 47 saturation and pressure vary in time and space. Under steady-state conditions, the fluids
 48 have established an equilibrium and macroscopic fluid properties are invariant in space
 49 (Tallakstad, Knudsen, et al., 2009). However, the prevailing theory of subsurface multiphase
 50 flows depends on the equivalency of underlying pore scale fluid dynamics during transient
 51 and steady-state flow.

52 The continuum framework for modelling multiphase subsurface flows assumes that each
 53 fluid phase will have its own designated pathway through the pore space, determined by capillary
 54 forces, whereby flow of that phase is independent of other fluids present (Armstrong
 55 et al., 2016; Blunt, 2017; Dullien, 1992). Thus, the fluid phase interfaces are assumed to
 56 be static, and the fluid configurations in equilibrium at the pore scale (Richards, 1931;
 57 Leverett, 1941). Changes to this pore scale arrangement to accommodate changes in sat-
 58 uration and pressure are assumed to occur rapidly relative to the macroscopic changes. A
 59 quasi-equilibrium state at the pore scale is thus assumed and flow properties are applied
 60 indiscriminately to steady and transient flows, as shown in Figure 1 a) in the context of
 61 modelling CO₂ plume migration during CO₂ storage. However, even during macroscopically
 62 steady-state flow, dynamic fluid interfaces have been observed when the non-wetting
 63 phase has a much lower viscosity than the wetting phase, such as CO₂ or natural gas displacing
 64 brine. While the average flow properties become invariant in time, there is a continual
 65 rearrangement, or intermittency, of fluid flow pathways at the pore scale (Tallakstad, Knud-
 66 sen, et al., 2009; Armstrong et al., 2016; Rücker et al., 2015; Spurin et al., 2019b, 2019a;
 67 Gao et al., 2019; Reynolds et al., 2017; Gao et al., 2020). Static interfaces have been ob-
 68 served between fluids within the pore space during steady-state flow when the non-wetting
 69 phase fluid viscosity is similar or higher than that of the wetting phase, such as crude oil
 70 displacing brine (Spurin et al., 2019a; Gao et al., 2017; Datta et al., 2014).

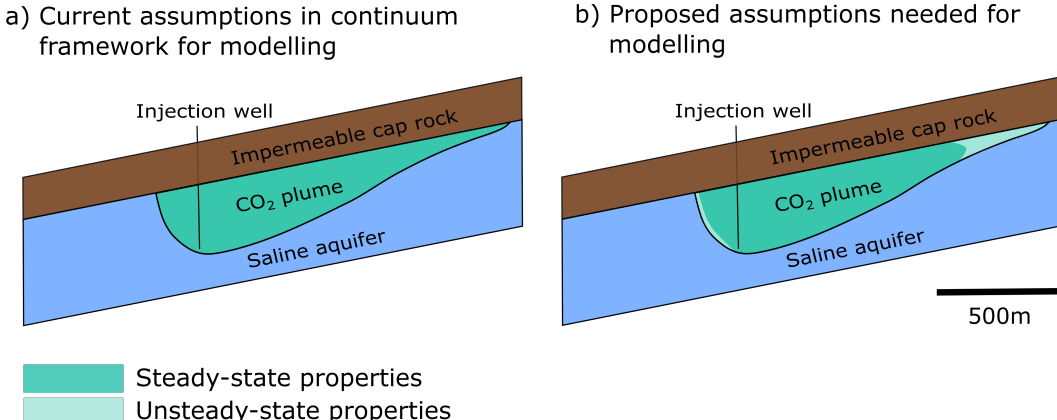


Figure 1. Schematic of the current subsurface modelling framework compared to a potential modelling framework applied here to study CO₂ migration and storage. The CO₂ plume shape was adapted from (MacMinn et al., 2010).

71 The existence of pore scale intermittency during steady-state flow suggests the possibility
 72 of even further complexity during transient flows more typical of the subsurface. This
 73 raises the possibility that unsteady-state flows should be modelled with separate upscaled
 74 constitutive laws or flow parameters. The transition to steady-state has been observed in
 75 2D glass micro models as a very rapid evolution after the fluid displacement front has passed
 76 (Tallakstad, Løvoll, et al., 2009). However, more complex fluid dynamics are generally ob-
 77 served in rocks (Armstrong et al., 2016; Rücker et al., 2015; Spurin et al., 2019b, 2019a; Gao
 78 et al., 2019; Reynolds et al., 2017; Gao et al., 2020). When a non-wetting phase invades a
 79 porous rock saturated with the wetting phase, the non-wetting phase travels in rapid, large
 80 bursts, referred to as Haines jumps (Haines, 1930; Berg et al., 2013; Bultreys et al., 2015).
 81 These rearrangements dissipate large amounts of energy (up to 64% of the input energy
 82 (Berg et al., 2013)), and heavily influence unsteady-state flow by altering the mobility of
 83 the non-wetting phase. Several theoretical models have been proposed to account for pore
 84 scale disequilibrium during transient flows with additional terms in the governing equations
 85 (Hassanizadeh et al., 1990; Barenblatt et al., 2003). These models typically introduce flow
 86 property dependencies on the rate of change in fluid saturation. However, their applicability,
 87 or the development of alternatives, has been limited by the difficulty in making observations
 88 at both the small length scales of rock pores and high time resolution of fluid displacement
 89 events.

90 With synchrotron X-ray micro computed tomography, we imaged pore scale fluid dy-
 91 namics with high time resolution (of 1 second) while macroscopic flow transitioned from
 92 transient to steady-state. We aim to establish if the pore scale fluid dynamics underpinning
 93 larger scale transient flow are distinguishable from the steady-state dynamics. If dis-
 94 tinguishable, transient flows may need to be modelled by distinct flow properties from those
 95 of steady-state flows, as demonstrated in Figure 1 b) for CO₂ plume migration during CO₂
 96 storage. To determine if transient flows have distinct flow properties requires observa-
 97 tions of the mobility of the fluid phases, and the connectivity of the flow network as the fluid
 98 configuration transitions to steady-state. This is explored for a non-wetting phase where
 99 intermittency would be expected at macroscopic steady-state (nitrogen) and a non-wetting
 100 phase where static interfaces would be expected at steady-state (decane). The non-wetting
 101 phase (nitrogen or decane) and the wetting phase (brine) were injected simultaneously into
 102 a permeable carbonate rock initially saturated with brine. This is a drainage process as the
 103 non-wetting phase initially has to displace brine to percolate across the rock sample. After

Experimental number	Non-wetting phase flow rate (ml/min)	Brine flow rate (ml/min)	Total flow rate (ml/min)	Fractional flow of brine (f_w)	Capillary number
1	0.015 (nitrogen)	0.085	0.1	0.85	1.6×10^{-7}
2	0.03 (nitrogen)	0.07	0.1	0.7	8.7×10^{-8}
3	0.05 (nitrogen)	0.05	0.1	0.5	5.4×10^{-8}
4	0.05 (decane)	0.05	0.1	0.5	2.2×10^{-6}

Table 1. Experimental parameters for the 4 experiments. Calculation of the capillary number is taken from (Spurin et al., 2019a) where $Ca = \frac{q}{\sigma\lambda}$. For a detailed explanation of the experimental procedure, please refer to the Supplementary Material.

104 this, an equilibrium in the pore scale fluid distribution is reached. To observe the transition
 105 to steady-state initiated with two fluid phases already percolating the pore space we also
 106 consider two further perturbations inducing unsteady-state for a nitrogen/brine system, by
 107 changing the relative flow rate of the fluids.

108 2 Results

109 There are four experiments described in this section. These experiments and their
 110 parameters are listed in Table 1. In experiment 1 we observed the transition to steady-
 111 state from the initial injection of nitrogen into a brine saturated rock. After steady-state
 112 had been achieved for experiment 1, and both fluids percolate through the pore space, the
 113 system is perturbed twice by changing the flow rate of brine and nitrogen (whilst the total
 114 flow rate remains the same); these changes represent experiments 2 and 3. The sample
 115 is then re-saturated with brine and the transition to steady-state is observed for decane
 116 injected simultaneously with brine; this is experiment 4. We determine macroscopic steady-
 117 state primarily through observations of the average pressure gradient across the rock sample,
 118 but also verify that average fluid saturation is unchanging.

119 2.1 Transition to a steady-state with intermittency

120 The nitrogen and brine were injected simultaneously into a rock saturated with brine
 121 (see Table 1 for experimental parameters). The flow was capillary dominated ($Ca = \frac{q}{\sigma\lambda} =$
 122 1.6×10^{-7} where q is the total Darcy flux, σ the interfacial tension between the non-wetting
 123 phase (nw) and brine, and λ the mobility) and the mobility ($\lambda = \frac{f_w}{\mu_{brine}} + \frac{1-f_w}{\mu_{nw}}$ where μ
 124 is the viscosity and f_w is the brine flow rate as a fraction of the total flow rate) indicated
 125 that intermittency was expected at steady-state (Spurin et al., 2019a). Macroscopic steady-
 126 state was determined based on the differential pressure across the rock sample (Figure 2).
 127 The pressure differential increased with the initial invasion of the non-wetting phase. It
 128 then continued to increase after the non-wetting phase had percolated across the rock,
 129 before finally plateauing and oscillating around a constant mean value with a period of
 130 approximately 10 minutes, which was considered steady-state.

131 Prior to percolation, the pressure increased monotonically (labels 1 and 2 in Figure 2)
 132 and there were large changes in gas saturation as gas was establishing a percolating path
 133 through the pore space. This did not induce major changes in the number of disconnected
 134 gas regions (ganglia), shown in Figure 3. The gas propagated in large bursts (Haines jumps
 135 (Haines, 1930; Berg et al., 2013; Bultreys et al., 2015)) that incorporated a large number of
 136 connected pores (Figure 4).

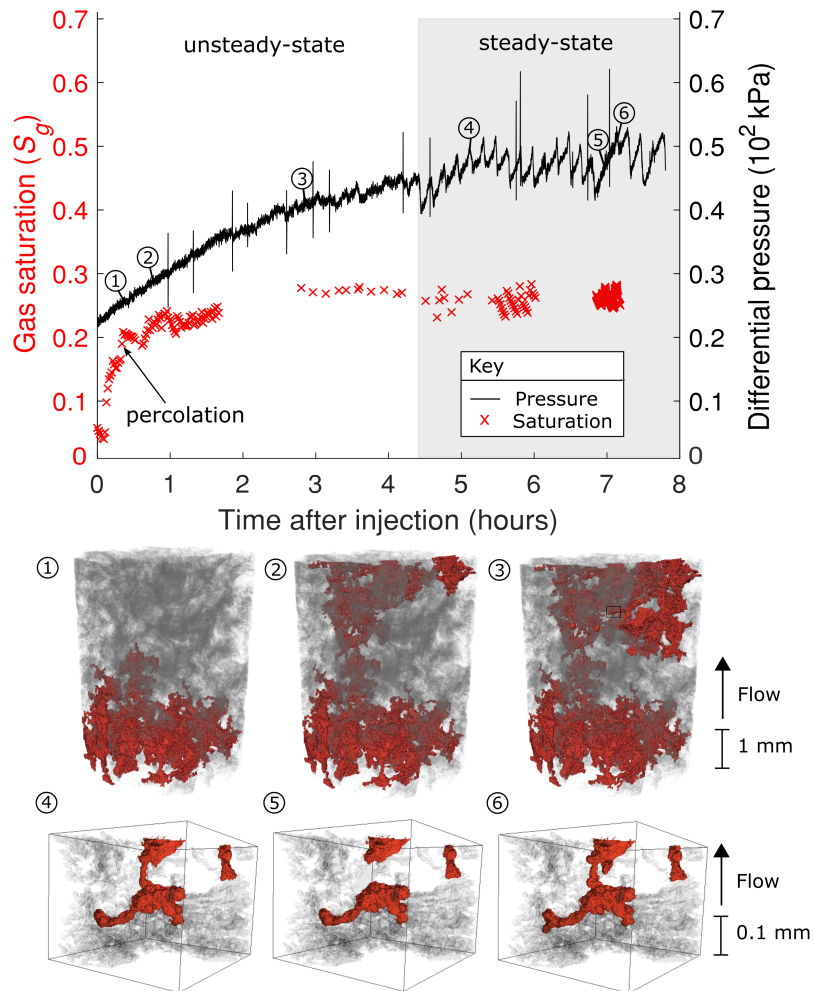


Figure 2. Top: the gas saturation and differential pressure time series following the initial perturbation (experiment 1 in Table 1). Bottom: images of the pore space at the indicated times in experiment 1. The gas is red, the brine is grey and the rock grains are transparent. The first three images are for the entire imaged section of the rock. At steady-state the dynamics are more subtle and so the final three images are zoomed in on a smaller region of the pore space indicated by a square in panel 3 See the supplementary information for videos of the dynamics.

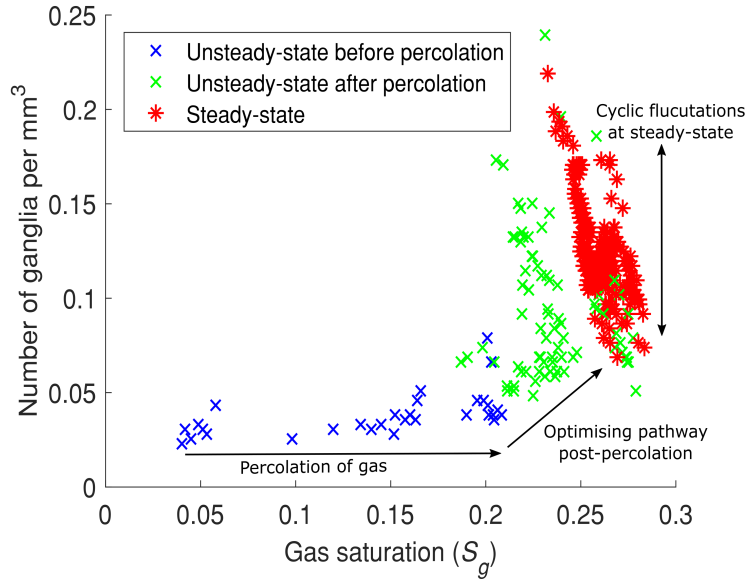


Figure 3. The gas saturation against the number of disconnected gas regions for experiment 1 - see Table 1 and Figure 2. At steady-state, there are many disconnection and reconnection events (intermittent pathway flow) resulting in a wide range in the connectivity in the gas, however, the saturation fluctuates over a much smaller range.

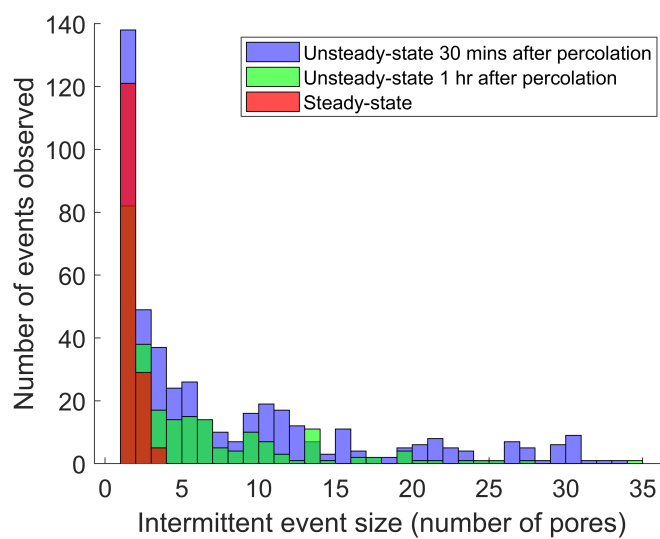


Figure 4. The size of an intermittently occupied part of the pore space decreases as we approach steady-state from the initial invasion (experiment 1 see Table 1 and Figures 2 and 3). The number of intermittent events also deceases.

137 After percolation but prior to steady-state, the gas saturation increased, but less
 138 rapidly than before percolation, and the number of disconnected gas regions increased as the
 139 pathway through the pore space was optimised (Figure 3). This change in flow behaviour
 140 corresponded to a decrease in the rate of change of the pressure differential in Figure 2.
 141 During the transition to steady-state, the average number of pores involved in an intermit-
 142 tent event decreased from greater than 30 pores to less than 5 (Figure 4). The total number
 143 of intermittent events also decreased (Figure 4). The number and size of intermittent events
 144 decreased as the gas found the optimal pathway through the system, but some flow pathways
 145 remained intermittent despite the flow being macroscopically steady-state flow, as shown by
 146 the pressure differential data (Figure 2).

147 At steady-state, the gas saturation plateaued and oscillated around an average value
 148 of $S_g = 0.26 \pm 0.02$, with a cycle lasting approximately 10 minutes in Figure 2; there was
 149 no net change in saturation when averaging over a differential pressure cycle. The number
 150 of disconnected gas regions fluctuated significantly (the range was $\pm 70\%$ of the mean)
 151 at steady-state, but the fluctuation in the saturation was much smaller (the range was \pm
 152 15% of the mean) (Figure 3). The size of the intermittent events was significantly lower
 153 than during the transition, generally involving only a single pore (Figures 4 and 2). This
 154 means that small changes at critical locations in the pore space led to major changes in the
 155 connectivity of the gas, demonstrated by the disconnecting and reconnecting of a region of
 156 gas from the main flow pathway by one periodic pathway that encompasses only one pore
 157 in panels 4-6 in Figure 2.

158 2.2 Transition to steady-state after a perturbation

159 The system was perturbed twice by changing the relative flow rates of the fluids while
 160 maintaining the total flow rate of gas and brine (experiments 2 and 3 in Table 1). A flow
 161 pathway had been established from the initial percolation (experiment 1), but by increasing
 162 the gas flow rate, the capillary pressure was increased and the gas was able to enter previously
 163 inaccessible pores. With this perturbation, the changes in system properties - pressure,
 164 saturation, intermittency - were more subtle than with the initial percolation (Figure 5).

165 Figure 6 shows that the majority of the pore space was continuously occupied by either
 166 brine or gas (less than 2% of the pore space was occupied intermittently by both phases).
 167 However, the impact of these intermittent flow pathways on the connectivity of the gas
 168 was significant, as shown in Figure 3. The peak for the amount of intermittent pathway
 169 flow during steady-state was observed when the brine flow rate constituted 70% of the total
 170 flow rate (experiment 2 in Figure 6, with details in Table 1). This agrees with previous
 171 observations of intermittency during steady-state flow (Spurin et al., 2019b). We therefore
 172 observed the transition to a state with more intermittent pathway flow (from experiment 1
 173 to experiment 2) and, subsequently, the transition to a state with less intermittent pathway
 174 flow (from experiment 2 to experiment 3).

175 When transitioning to steady-state for experiment 2, where the steady-state intermit-
 176 tency is more than the previous step, we observe a gradual increase in gas saturation and
 177 intermittency (Figures 5 and 6, respectively). This makes this transition markedly different
 178 from the initial percolation (experiment 1), where the dynamics were largest at the onset,
 179 and then reduced to small movements (Figure 4). Many of the flow pathways were estab-
 180 lished during the initial percolation phase and so the transition to steady-state was quicker.
 181 The modest increase in intermittency is associated with the opening of new pathways to
 182 accommodate the greater gas flux. The long period (approximately 10 minute) pressure
 183 differential oscillations persist through the perturbation (Figure 5).

184 When transitioning to steady-state for experiment 3, where the steady-state intermit-
 185 tency is less than the previous step, we observe an increase in gas saturation and a gradual
 186 decrease in intermittency (Figures 5 and 6, respectively). The transition to steady-state is
 187 quickest for this experiment (Figure 5).

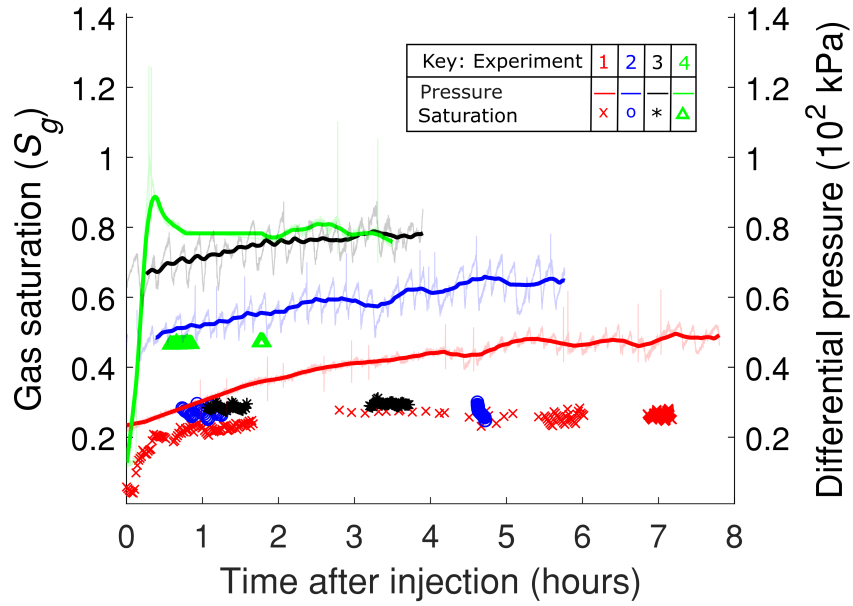


Figure 5. The gas saturation and differential pressure as a function of time. The raw pressure data is shown in light colouring while the bold colouring shows the pressure data averaged over a period of an oscillation to clearly show the transition to steady-state. See Table 1 for the experimental parameters.

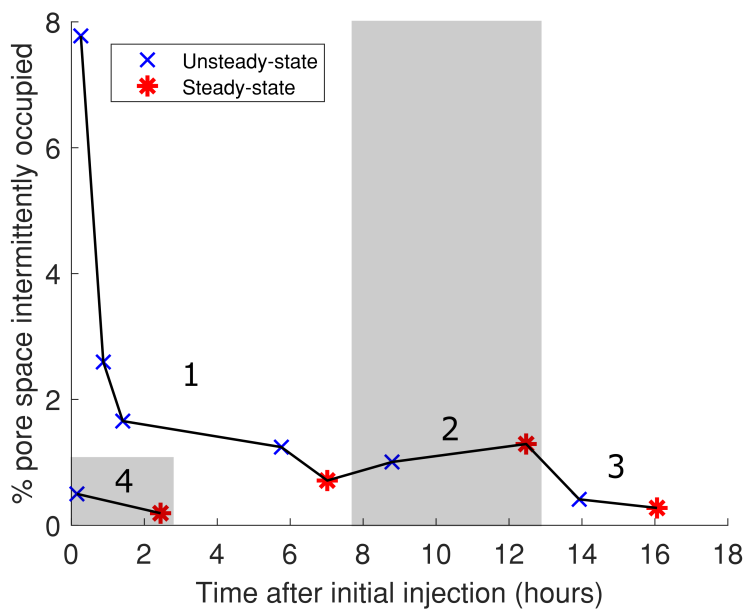


Figure 6. The percentage volume of the pore space identified as intermittent. Each point is the average of 10 minute window of continuous imaging. The different experiments (as listed in Table 1) are labelled on the image.

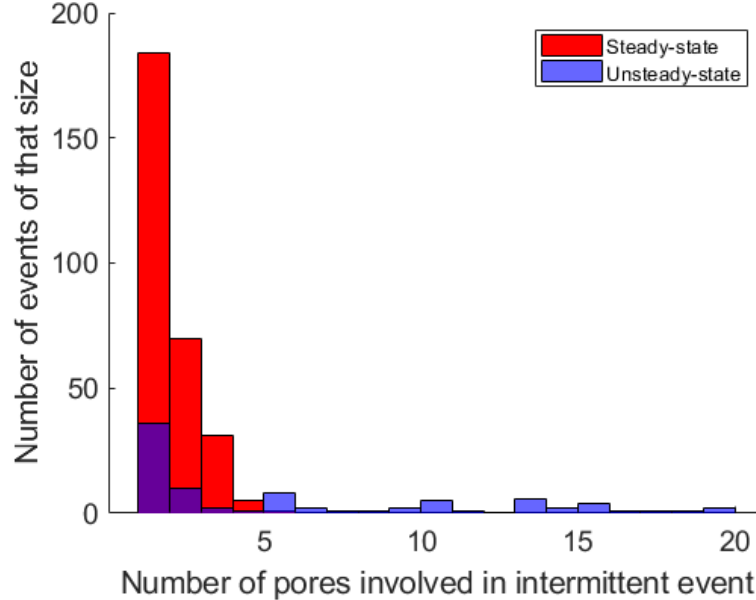


Figure 7. The size of an intermittently occupied part of the pore space decreases as we approach steady-state for experiment 2, where a perturbation was initiated in a steady state percolating system by changing the relative flow rates of nitrogen and brine. Figure 4 is the equivalent figure but for experiment 1. Similar evolutions are observed for experiments 3 and 4.

Overall, transitions to steady state after an initial percolation had occurred are characterised by gradual changes in intermittency between an initial and final saturation state regardless of whether the intermittency is increasing or decreasing. However, even with little change in saturation the size of intermittent events is much larger during the transient than steady-state flow, similar to observations made during the initial percolation (Figure 7). It is thus a general feature of flow during both the initial percolation and subsequent perturbations that unsteady-state movements incorporate larger events (up to 20 pores involved in an intermittent event) whereas steady-state pathways involve much smaller events (always less than 5 pores) (Figure 7).

2.3 Transition to a steady-state with no intermittency

The sample was re-saturated with brine and an experiment was conducted with decane as the non-wetting phase to explore the role of viscosity on the transition to steady-state (experiment 4 in Table 1). The viscosity ratio has been identified as a primary variable controlling intermittency, with less dynamics expected at steady-state for systems with more viscous non-wetting fluids (Spurin et al., 2019b). The flow rate was matched with the gas experiments and the capillary number is higher by an order of magnitude due to the viscosity of the oil (although flow is still capillary dominated, Table 1).

The initial transition to steady-state was much quicker (taking less than an hour) than with gas, shown in Figures 5 and 6. The oil saturation is higher than the gas saturation in experiment 3 as expected from increasing the non-wetting phase viscosity (Figure 5). The fluctuations in pressure are much smaller than for the gas experiments. We do observe intermittency during the transition to steady-state. However, it is far less prevalent than during the initial nitrogen percolation (Figure 6) and it evolves more quickly (Figure 5).

211 As expected, there is almost no intermittency at steady-state (0.2% of the pore space is
 212 identified as intermittent).

213 3 Conclusions

214 Intermittent fluid flow pathways were always observed during macroscopically transient
 215 flow. These intermittent flow pathways constituted a larger volume of the pore space and
 216 were most frequent after the initial invasion of the fluids and were distinct from steady-state
 217 intermittent pathways by size and frequency.

218 The mobility of the non-wetting phase was observed to be different during transient
 219 flow. The change in saturation after percolation was small (the saturation was already
 220 88% of the steady-state saturation at the time of percolation), but there was a much larger
 221 increase in pressure (the differential pressure was 70% of the steady-state differential pressure
 222 at percolation). This means that the change in saturation per unit time is smaller than the
 223 change in the total mobility of the fluids per unit time (which is inversely proportional to
 224 the pressure drop). The mobility of the non-wetting phase, for a given saturation, is higher
 225 for a lower differential pressure. This implies that the non-wetting phase was more mobile in
 226 the transitional stage than at steady-state and that intermittency is associated with higher
 227 mobility of the non-wetting fluid phase. These results suggest that transient flow dynamics
 228 should not be modelled using steady-state flow properties. However, current models that do
 229 consider dynamic effects suggest these effects may be parameterised by rates of change of
 230 fluid saturation (Barenblatt et al., 2003; Hassanzadeh et al., 2002). This approach cannot
 231 be applied to our experiments because the saturation remains approximately constant while
 232 the total mobility changes significantly.

233 We estimate the length scale in the fluid plume front from which steady-state dynamics
 234 can be assumed and applied to scenarios, such as in Figure 1 b). Steady-state was achieved
 235 after the initial invasion in experiment 1 after approximately 180 pore volumes of gas were
 236 injected through a sample 20 mm in length. This would correspond to a plume front
 237 governed by transient flow dynamics approximately 3.6 m thick. For experiment 4, steady-
 238 state was achieved after approximately 60 pore volumes of gas were injected, corresponding
 239 to a distance of approximately 0.9 m. This means the transition zone would be much
 240 smaller for systems such as conventional and heavy oil, and NAPL contamination, where
 241 intermittency is not expected at subsurface flow conditions.

242 There are added complexities in subsurface applications if the injected phase is already
 243 present, or if the plume is layered due to geological constraints. Firstly, if the non-wetting
 244 phase is already present, then the transition to steady-state is less evident than it was for
 245 the initial invasion of gas. Changing the flow parameters once the non-wetting phase had
 246 percolated the pore space resulted in gradual changes in saturation and intermittency as a
 247 new steady-state was established. Secondly, for the Sleipner CO₂ plume, as an example, the
 248 plume exists as layers that are frequently 1-5 m thick (R. Chadwick et al., 2009). Our work
 249 suggests that the leading edge of the CO₂ plume in the unsteady-state regime is indeed more
 250 mobile than would be predicted by current quasi-steady-state models. This effect would be
 251 more noticeable in a layered plume with multiple plume fronts. These complexities may
 252 provide an explanation to why predictive modelling subsurface fluid flows at field relevant
 253 scales (100 - 1000m) is notoriously difficult, exemplified by the many attempts to model
 254 CO₂ plume migration in a saline aquifer at Sleipner (Williams & Chadwick, 2017; Singh et
 255 al., 2010; R. A. Chadwick & Noy, 2015; Zhu et al., 2015; Cavanagh & Haszeldine, 2014).
 256 Existing models that include transient dynamics focus on the rate dependence of satura-
 257 tion or capillary pressure, which do not necessarily change significantly in this transition
 258 (Barenblatt et al., 2003; Hassanzadeh et al., 2002, 1990; Picchi & Battiaio, 2018). Hence,
 259 we suggest that a new modelling framework should be explored to account for the behaviour
 260 we have observed.

261 4 Materials and Methods

262 The experiments were conducted in a cylindrical Estaillades sample, 5 mm diameter
 263 and 20 mm length. The sample was attached to a dual injection piece, specifically designed
 264 for the simultaneous injection of two fluid phases while suppressing the generation of slug
 265 flow. The sample was initially saturated with brine (deionised water doped with 15% wt.
 266 KI to improve the X-ray contrast). The system was pressurised to 8 MPa to minimise the
 267 compressibility of nitrogen, with an additional 2 MPa of confining pressure. Then both
 268 nitrogen and brine were injected simultaneously, with the flow rates of the nitrogen and the
 269 brine listed in Table 1. A differential pressure transducer (Keller, 300 kPa transducer with
 270 1.5 kPa accuracy) was connected across the sample, to measure the pressure drop. Steady-
 271 state was determined to be reached once the differential pressure had plateaued. The sample
 272 was resaturated with brine at the end of the nitrogen experiments, and the experiment was
 273 repeated with decane and brine injected simultaneously.

274 The X-ray imaging was conducted at the TOMCAT beamline at the Swiss Light
 275 Source, Paul Scherrer Institut, Villigen, Switzerland. The sample was exposed to filtered
 276 polychromatic X-ray radiation with a peak energy of about 26 keV originating from a 2.9
 277 T bending magnet source. The filter was 2300 μm -thick Silicon. An in-house developed
 278 GigaFRoST camera (Mokso et al., 2017) and a high numerical aperture white-beam mi-
 279 croscope (Optique Peter) with 4x magnification (Bührer et al., 2019) were used, yielding
 280 an effective pixel size of 2.75 μm . Each tomogram contained 1000 projections over 180°
 281 rotation. Each scan lasted 1 s, with a further 1 s required for the sample to rotate back to
 282 its initial position before the next scan could begin.

283 Each image analysed was $4224 \times 4298 \times 4263 \mu\text{m}$ in size. The images were recon-
 284 structed from the X-ray projections using the propagation-based phase contrast method
 285 (Paganin et al., 2002) and the gridrec algorithm (Marone & Stampanoni, 2012). The im-
 286 ages were then filtered with a non-local means filter to suppress noise whilst maintaining
 287 the information at phase boundaries (Schlüter et al., 2014). The first image was taken with
 288 just deionised water in the pore space. This image is used to segment the pore space from
 289 the rock grains using a watershed segmentation algorithm (Beucher & Meyer, 1993). Then
 290 the sample was saturated with the brine, and another image was taken; this is the brine
 291 saturated imaged. All subsequent images with the non-wetting phase (nitrogen or decane)
 292 and brine present were subtracted from the brine saturated image, this results in a differ-
 293 ential image whereby only the location of non-wetting phase remains. From this a simple
 294 greyscale value threshold can be used to segment out the nitrogen. The pore space was
 295 overlain on this segmentation to locate the pore space occupied with brine.

296 The pore space morphology was extracted using a maximal inscribed spheres (max-
 297 imum ball, MB) network extraction technique (Dong & Blunt, 2009; Raeini et al., 2017).
 298 The fluid occupancy for each pore MB was assigned for every time step. Then for every
 299 pore, the neighbouring pores are listed with their occupancy. Using this, the size of an
 300 intermittent can be calculate, resulting in Figures 4 and 7.

301 References

- 302 Armstrong, R. T., McClure, J. E., Berrill, M. A., Rücker, M., Schlüter, S., & Berg, S.
 303 (2016). Beyond Darcy's law: The role of phase topology and ganglion dynamics for
 304 two-fluid flow. *Physical Review E*, 94(4), 043113.
- 305 Bachu, S. (2000). Sequestration of CO₂ in geological media: criteria and approach for site
 306 selection in response to climate change. *Energy Conversion and Management*, 41(9),
 307 953–970.
- 308 Barenblatt, G., Patzek, T. W., & Silin, D. (2003). The mathematical model of nonequilib-
 309 rium effects in water-oil displacement. *SPE journal*, 8(04), 409–416.
- 310 Berg, S., Ott, H., Klapp, S. A., Schwing, A., Neiteler, R., Brussee, N., ... others (2013).

- 311 Real-time 3D imaging of haines jumps in porous media flow. *Proceedings of the Na-*
 312 *tional Academy of Sciences*, 110(10), 3755–3759.
- 313 Beucher, S., & Meyer, F. (1993). The morphological approach to segmentation: the water-
 314 shed transformation. *Mathematical morphology in image processing*, 34, 433–481.
- 315 Bickle, M. J. (2009). Geological carbon storage. *Nature Geoscience*, 2(12), 815–818.
- 316 Blunt, M. J. (2017). *Multiphase flow in permeable media: A pore-scale perspective*. Cam-
 317 bridge University Press.
- 318 Bührer, M., Stampanoni, M., Rochet, X., Büchi, F., Eller, J., & Marone, F. (2019). High-
 319 numerical-aperture macroscope optics for time-resolved experiments. *Journal of syn-*
 320 *chrotron radiation*, 26(4).
- 321 Bultreys, T., Boone, M. A., Boone, M. N., De Schryver, T., Masschaele, B., Van Loo, D.,
 322 ... Cnudde, V. (2015). Real-time visualization of Haines jumps in sandstone with
 323 laboratory-based microcomputed tomography. *Water Resources Research*, 51(10),
 324 8668–8676.
- 325 Cavanagh, A. J., & Haszeldine, R. S. (2014). The Sleipner storage site: Capillary flow
 326 modeling of a layered CO₂ plume requires fractured shale barriers within the Utsira
 327 Formation. *International Journal of Greenhouse Gas Control*, 21, 101–112.
- 328 Chadwick, R., Noy, D., Arts, R., & Eiken, O. (2009). Latest time-lapse seismic data
 329 from Sleipner yield new insights into CO₂ plume development. *Energy Procedia*, 1(1),
 330 2103–2110.
- 331 Chadwick, R. A., & Noy, D. J. (2015). Underground CO₂ storage: demonstrating reg-
 332 ulatory conformance by convergence of history-matched modeled and observed CO₂
 333 plume behavior using Sleipner time-lapse seismics. *Greenhouse Gases: Science and*
 334 *Technology*, 5(3), 305–322.
- 335 Datta, S. S., Ramakrishnan, T., & Weitz, D. A. (2014). Mobilization of a trapped non-
 336 wetting fluid from a three-dimensional porous medium. *Physics of Fluids*, 26(2),
 337 022002.
- 338 Dong, H., & Blunt, M. J. (2009). Pore-network extraction from micro-computerized-
 339 tomography images. *Physical Review E*, 80(3), 036307.
- 340 Dullien, F. A. (1992). *Porous media: fluid transport and pore structure*. Academic Press.
- 341 Gao, Y., Lin, Q., Bijeljic, B., & Blunt, M. J. (2017). X-ray microtomography of intermit-
 342 tency in multiphase flow at steady state using a differential imaging method. *Water*
 343 *Resources Research*, 53(12), 10274–10292.
- 344 Gao, Y., Lin, Q., Bijeljic, B., & Blunt, M. J. (2020). Pore-scale dynamics and the multiphase
 345 darcy law. *Physical Review Fluids*, 5(1), 013801.
- 346 Gao, Y., Raeini, A. Q., Blunt, M. J., & Bijeljic, B. (2019). Pore occupancy, relative
 347 permeability and flow intermittency measurements using X-ray micro-tomography in
 348 a complex carbonate. *Advances in Water Resources*, 129, 56–69.
- 349 Haines, W. B. (1930). Studies in the physical properties of soil. v. the hysteresis effect in
 350 capillary properties, and the modes of moisture distribution associated therewith. *The*
 351 *Journal of Agricultural Science*, 20(1), 97–116.
- 352 Hassanizadeh, S. M., Celia, M. A., & Dahle, H. K. (2002). Dynamic effect in the capillary
 353 pressure–saturation relationship and its impacts on unsaturated flow. *Vadose Zone*
 354 *Journal*, 1(1), 38–57.
- 355 Hassanizadeh, S. M., Gray, W. G., et al. (1990). Mechanics and thermodynamics of mul-
 356 tiphase flow in porous media including interphase boundaries. *Adv. Water Resour.*,
 357 13(4), 169–186.
- 358 Leverett, M. (1941). Capillary behavior in porous solids. *Transactions of the AIME*,
 359 142(01), 152–169.
- 360 MacMinn, C. W., Szulczewski, M. L., & Juanes, R. (2010). CO₂ migration in saline
 361 aquifers. Part 1. capillary trapping under slope and groundwater flow. *Journal of*
 362 *Fluid Mechanics*, 662, 329–351.
- 363 Marone, F., & Stampanoni, M. (2012). Regridding reconstruction algorithm for real-time
 364 tomographic imaging. *Journal of synchrotron radiation*, 19(6), 1029–1037.
- 365 Mokso, R., Schlepütz, C. M., Theidel, G., Billich, H., Schmid, E., Celcer, T., ... oth-

- 366 ers (2017). Gigafrost: the gigabit fast readout system for tomography. *Journal of*
 367 *synchrotron radiation*, 24(6), 1250–1259.
- 368 Paganin, D., Mayo, S. C., Gureyev, T. E., Miller, P. R., & Wilkins, S. W. (2002). Simulta-
 369 neous phase and amplitude extraction from a single defocused image of a homogeneous
 370 object. *Journal of microscopy*, 206(1), 33–40.
- 371 Picchi, D., & Battiato, I. (2018). The impact of pore-scale flow regimes on upscaling of
 372 immiscible two-phase flow in porous media. *Water Resources Research*, 54(9), 6683–
 373 6707.
- 374 Pye, V. I., & Patrick, R. (1983). Ground water contamination in the United States. *Science*,
 375 221(4612), 713–718.
- 376 Raeini, A. Q., Bijeljic, B., & Blunt, M. J. (2017). Generalized network modeling: Network
 377 extraction as a coarse-scale discretization of the void space of porous media. *Physical*
 378 *Review E*, 96(1), 013312.
- 379 Reynolds, C. A., Menke, H., Andrew, M., Blunt, M. J., & Krevor, S. (2017). Dynamic fluid
 380 connectivity during steady-state multiphase flow in a sandstone. *Proceedings of the*
 381 *National Academy of Sciences*, 114(31), 8187–8192.
- 382 Richards, L. A. (1931). Capillary conduction of liquids through porous mediums. *Physics*,
 383 1(5), 318–333.
- 384 Rubin, E., & De Coninck, H. (2005). IPCC special report on carbon dioxide capture and
 385 storage. UK: Cambridge University Press. TNO (2004): *Cost Curves for CO₂ Storage*,
 386 Part, 2, 14.
- 387 Rücker, M., Berg, S., Armstrong, R., Georgiadis, A., Ott, H., Schwing, A., . . . others (2015).
 388 From connected pathway flow to ganglion dynamics. *Geophysical Research Letters*,
 389 42(10), 3888–3894.
- 390 Schlüter, S., Sheppard, A., Brown, K., & Wildenschild, D. (2014). Image processing of
 391 multiphase images obtained via X-ray microtomography: a review. *Water Resources*
 392 *Research*, 50(4), 3615–3639.
- 393 Singh, V. P., Cavanagh, A., Hansen, H., Nazarian, B., Iding, M., & Ringrose, P. S. (2010).
 394 Reservoir modeling of CO₂ plume behavior calibrated against monitoring data from
 395 Sleipner, Norway. In *Spe annual technical conference and exhibition* (Vol. 134891).
- 396 Spurin, C., Bultreys, T., Bijeljic, B., Blunt, M. J., & Krevor, S. (2019a). Mechanisms
 397 controlling fluid break-up and reconnection during two-phase flow in porous media.
 398 *Physical Review E*, 100(4), 043115.
- 399 Spurin, C., Bultreys, T., Bijeljic, B., Blunt, M. J., & Krevor, S. (2019b). Intermittent
 400 fluid connectivity during two-phase flow in a heterogeneous carbonate rock. *Physical*
 401 *Review E*, 100(4), 043103.
- 402 Tallakstad, K. T., Knudsen, H. A., Ramstad, T., Løvoll, G., Måløy, K. J., Toussaint, R., &
 403 Flekkøy, E. G. (2009). Steady-state two-phase flow in porous media: statistics and
 404 transport properties. *Physical Review Letters*, 102(7), 074502.
- 405 Tallakstad, K. T., Løvoll, G., Knudsen, H. A., Ramstad, T., Flekkøy, E. G., & Måløy, K. J.
 406 (2009). Steady-state, simultaneous two-phase flow in porous media: An experimental
 407 study. *Physical Review E*, 80(3), 036308.
- 408 Williams, G. A., & Chadwick, R. A. (2017). An improved history-match for layer spreading
 409 within the Sleipner plume including thermal propagation effects. *Energy Procedia*,
 410 114, 2856–2870.
- 411 Zhu, C., Zhang, G., Lu, P., Meng, L., & Ji, X. (2015). Benchmark modeling of the Sleipner
 412 CO₂ plume: Calibration to seismic data for the uppermost layer and model sensitivity
 413 analysis. *International Journal of Greenhouse Gas Control*, 43, 233–246.

414 **Acknowledgments**

415 We acknowledge the Paul Scherrer Institut, Villigen, Switzerland for provision of synchrotron
 416 radiation beamtime at the TOMCAT beamline X02DA of the SLS. Catherine Spurin is
 417 grateful for her funding through the President's PhD Scholarship, Imperial College London.
 418 Tom Bultreys acknowledges the Research Foundation-Flanders (FWO) for his post-doctoral

manuscript submitted to *Water Resources Research*

419 fellowship 12X0919N. We are grateful to all our colleagues within the Shell Digital Rocks
420 Programme for their useful discussions and support. Vladimir Novak acknowledges funding
421 from the European Union's Horizon 2020 research and innovation programme under the
422 Marie Skłodowska-Curie Grant Agreement No 701647. We acknowledge John Spurin and
423 Jane Spurin for transporting experimental equipment and Alessio Scanziani for his help
424 during the experiments.

© 2020. This work is licensed under
<http://creativecommons.org/licenses/by/4.0/legalcode> (the “License”).
Notwithstanding the ProQuest Terms and Conditions, you may use this
content in accordance with the terms of the License.